SLAC-PUB-16300

Kinetics and fracture resistance of lithiated silicon nanostructure pairs controlled by their mechanical interaction

Seok Woo Lee[1,a], Hyun-Wook Lee[2,a], Ill Ryu[3], William D. Nix[2], Huajian Gao[3], Yi Cui[2,4*]

[1]Geballe Laboratory for Advanced Materials, Stanford University, Stanford, California 94305, USA

[2]Department of Materials Science and Engineering, Stanford University, Stanford, California 94305, USA

[3]School of Engineering, Brown University, Providence, Rhode Island 02912, USA

[4]Stanford Institute for Materials and Energy Sciences, SLAC National Accelerator Laboratory, 2575 Sand Hill Road, Menlo Park, California 94025, USA

[a]These authors contributed equally to this work

[*]Corresponding author. E-mail: yicui@stanford.edu

Abstract

Following an explosion of studies of silicon as a negative electrode for Li-ion batteries, the anomalous volumetric changes and fracture of lithiated single Si particles have attracted significant attention in various fields, including mechanics. However, in real batteries, lithiation occurs simultaneously in clusters of Si in a confined medium. Hence, understanding how the individual Si structures interact during lithiation in a closed space is necessary. Herein, we demonstrate physical/mechanical interactions of swelling Si structures during lithiation using well-defined Si nanopillar pairs. *Ex situ* SEM and *in situ* TEM studies reveal that compressive stresses change the reaction kinetics so that preferential lithiation occurs at free surfaces when the pillars are mechanically clamped. Such mechanical interactions enhance the fracture resistance of

This material is based upon work supported by the U.S. Department of Energy, Office of Science, Office of Basic Energy Sciences, Division of Materials Sciences and Engineering, under Contract No. DE-AC02-76SF00515.

lithiated Si by lessening the tensile stress concentrations in Si structures. This study will contribute to improved design of Si structures at the electrode level for high performance Li-ion batteries.

Introduction

Silicon (Si) has attracted great attention as a promising negative electrode material for Li-ion batteries due to its exceptional theoretical specific capacity of 3578 mAh g^{-1} for the $Li_{15}Si_4$ phase at room temperature[1–5]. Despite these preeminent theoretical properties, conventional Si anodes face significant challenges due to the large volume changes that accompany lithiation. These effects have limited the choice of Si as a commercial negative electrode because they can lead to the loss of electrical contact between active materials by mechanical fracture, accumulation of solid-electrolyte interphase (SEI) layers, and rapid capacity fading during electrochemical cycling[6–9]. Recently, nanotechnology has achieved a breakthrough to overcome the aforementioned challenges of Si as a negative electrode for Li-ion batteries[1,2]. Various Si nanomaterials and engineered Si nanostructures such as nanowires/particles, hollow spheres, and porous nanostructures have demonstrated stable cycling and resistance to fracture in spite of the large volume change of Si[1,10–12]. Engineered nanostructures, wherein the surface of the Si structure does not strain and where a gap for volume expansion of lithiated Si is provided, lead to a stable SEI layer formation on the surface of the electrode material and enhanced Coulombic efficiency and dramatically improved cycle life[7,8].

Accompanying the search for high performance Si anodes, fundamental studies have provided a better idea of how Si lithiates, swells and fractures, leading to a basis for the rational design of Si structures[4]. Especially, the extreme volumetric and structural changes of lithiated Si have attracted much attention in mechanics because of the large stress evolution and corresponding mechanical fracture. The dramatic change of mechanical properties by lithiation has been documented by simulations and

experiments[13–18]. Analytical and numerical analyses, including both elasticity and plasticity, have suggested both diffusion induced stress models and pressurized hollow structure models of lithiation/delithiation of Si as a part of an effort to explain how the expansion causes stress evolution and mechanical fracture[19–24]. These models are based on experimental observations such as volumetric changes, mechanical fracture, and structural changes[25–28]. Recently, top-down fabrication of Si nanostructures allowed the systematic study of the effects of crystal orientation, dimensions, and morphology which revealed preferential lithiation along <110> directions of crystalline Si, a size dependence of the fracture resistance, and the robustness of amorphous Si[6,29–33]. *In situ* transmission electron microscopy (TEM) has provided time-series crystallographic and chemical information as well as information about the morphology of lithiated Si[34]. The observed dynamic behavior of Si nanostructures provided information about the kinetics of lithiation controlled by mechanical stresses and the orientation of the reaction interface of crystalline Si as well as the aforementioned anisotropic expansion and fracture behavior[35–39].

However, in a real battery system, Si structures form as clusters at the electrode level and the lithiation of the individual structures occurs simultaneously in a confined medium. Then, swelling Si structures in fixed volume mechanically interact with each other and the reaction kinetics and fracture behavior become more complicated than that observed for single-particle systems. Therefore, understanding how the individual Si structures mechanically interact during lithiation is necessary for the rational design of Si electrodes. Here, we show how mechanical interactions of neighboring crystalline Si structures affect their reaction kinetics and fracture resistance during electrochemical lithiation, using *ex situ* scanning electron microscopy (SEM) and *in situ* TEM of Si nanopillar pairs.

Results

Lithiation of mechanically clamped Si pillar

In order to mimic the cluster of crystalline Si particles in the confined volume in the negative electrode of a Li-ion battery, Si nanopillars with adjacent rigid walls were fabricated by e-beam lithography and dry etching of <110> single crystalline Si wafer (See Methods and Supplementary Fig. 1a-c). We used <110> Si pillars so that lateral volume expansion would occur preferentially along two opposite <110> directions upon lithiation. To simulate mechanical clamping of Si structure in closed-packed media, e-beam lithography defined the various diameters of the pillars and the location of rigid walls for two different geometries so that rigid walls block both sides of <110> direction of the pillar. For the *ex situ* SEM study, the fabricated silicon nanopillar and wall array on a piece of wafer was lithiated by sweeping voltage down to 10 mV vs. Li/Li^+ and held for more than 10 hours in a half-cell with Li foil (see Methods and Supplementary Fig. 1d-i). For the *in situ* TEM study, the pillars were placed at the edge <110> direction of the piece of <110> wafer and mounted on the TEM holder with a proper tilting so that the pillar can be observed under e-beam without shading (see Supplementary Fig. 2). After building the solid cell configuration with a Li/Li_2O counter electrode, the pillar is lithiated by applying DC bias during the TEM observation.

In order to simulate the mechanical clamping of Si structures in closed-packed media, a pillar was prepared between two rigid walls blocking both <110> directions upon lithiation as shown in Fig. 1. A <110> Si pillar 550 nm in diameter standing between two rigid walls with 320 nm gaps was fabricated for the SEM study (Fig. 1a). Since the crystal orientation is identical to the first case, the pillar and the walls expand laterally along <110> directions and fill the gap between them upon lithiation. After the contact, the lithiation along the <110> direction cannot proceed due to the build-up of compressive stresses and the pillar lithiates along a second favored direction, <100> as shown in Fig. 1b. The walls

also expand along the <100> direction after contact with the pillar. Fig. 1c compares dimension changes of the unclamped and clamped <110> pillars. The unclamped pillar with a diameter of 0.36 μm expands to 1.25 and 0.54 μm along <110> and <100> directions, respectively, upon lithiation, as found in our previous study[30]. The unclamped pillar clearly shows anisotropic expansion behavior where the <110> direction exhibits a faster reaction than the <100> direction. In contrast, the clamped pillar with a diameter of 0.55 μm expands to 0.88 and 1.06 μm along the <110> and <100> directions, respectively, upon lithiation. Ideally, the swelling pillar and wall would come into contact in the middle of the gap and the width of the pillar along the <110> direction would then be 0.87 μm (= original diameter + 2 × gap / 2), which is indeed very close to the measured width. Therefore, it is clear that the lithiation along the <110> direction is stopped at the point of contact and the subsequent lithiation continues along the <100> direction.

In situ TEM observation of the <110> Si pillar near the wall provides a better picture of the dynamic lithiation behavior of the crystalline Si core and the corresponding mechanical interaction. The electron beam penetrates through the <100> direction of the <110> Si nanopillar standing by the rigid wall, so a lateral <110> expansion of the nanopillar can be monitored during the lithiation process (Fig. 2a, b). The reaction stoppage of the pillar after the contact is clearly shown in the *in situ* TEM study. For the mechanical clamping, three <110> Si nanopillars with the same diameters of 550 nm and rigid walls on either side of the pillars were fabricated as shown in Fig. 2b. A single pillar clamped by two rigid walls also exhibits termination of the expansion as shown in *ex situ* SEM, but overlapping of structures hindered precise measurement (see Supplementary Movie 1). The time-series of TEM images of the lithiating pillars clamped by the walls are shown in Fig. 2c-e (see also Supplementary Movies 2 and 3). At the beginning of the lithiation, the pillars start to expand as a normal <110> single pillar does in spite of inconsistent expansion due to irregular contact with Li metal (c and d). After the contact, a Li_xSi shell

fills the empty space and the crystalline Si core stops shrinking due to the termination of the lithiation (e). The plot of the diameters of the Li_xSi outer shell and the crystalline Si core as a function of time clearly shows that the expansion of the shell and shrinkage of the core are slowing down upon the contact and halted at about 90 seconds (Fig. 2f). Since then, the diameter of the remaining crystalline core is maintained for over 400 seconds and the lithiation cannot proceed further along <110> direction against the neighboring pillars due to the mechanical clamping. In contrast, unclamped pillar exhibits the completed lithiation and the mechanical fracture without the termination of the lithiation (see Supplementary Movies 4 and 5).

Analytical model

In order to explain how mechanical clamping stops the lithiation at the contact, an analytical model is developed by considering mechanical stress evolution upon the clamping and change of driving force of the reaction. The driving force of the lithiation is defined as:

$$\Delta G = \Delta G_r^{Li_xSi} - e\Phi + \Delta G_\sigma \quad (1)$$

where ΔG is the change of Gibbs free energy, ΔG_r^{LixSi} is the change of free energy of lithiation without applied voltage or mechanical stress, Φ is the applied voltage to the electrochemical cell, and ΔG_σ is the change of free energy due to mechanical stress[21]. ΔG_σ expresses the relationship between mechanical stress at the atomically sharp interface of crystalline Si and swelling Li_xSi alloy and the change of the driving force of the reaction[28]. Considering the consumption of one Li atom to form $1/x$ units of Li_xSi, ΔG_σ is computed as[21,35]:

$$\Delta G_\sigma = \frac{1}{x}\left(\sigma_m^{Si}\Omega^{Si} - \sigma_m^{Li_xSi}\Omega^{Li_xSi}\right) \quad (2)$$

where σ_m^{Si} and σ_m^{LixSi} are the mean stresses in the crystalline Si and in the Li_xSi at the interface, respectively, and Ω^{Si} and Ω^{LixSi} are the volumes per Si atom and unit of Li_xSi, respectively. Since a

negative ΔG drives lithiation, compressive hydrostatic stress in the crystalline Si or tensile hydrostatic stress in the Li_xSi enhances lithiation process. The model for the estimation of stress upon lithiation includes consideration of both the 'Before contact' and 'After contact' of neighboring Si structures. Fig. 3a shows a schematic view of the model of 'Before contact'. A square <110> Si pillar of $2t_0$ width is located between two fixed rigid wall structures aligned along the lateral <110> direction with a gap of g. Assuming dominant expansion and propagation of flat {110} interface along the <110> direction as shown in the previous studies[31], after lithiation the thicknesses of crystalline Si core and the Li_xSi layer may be called t_{Si} and t_{LixSi}, respectively. Also t_1 (=t_{LixSi}/4) is the thickness of the consumed crystalline Si and t_2 is the displacement of each surface toward each other. Before the structures contact each other, Li_xSi in the gap is free to expand laterally along the <110> direction, which is normal to the interface, so the normal stress (σ_n) is zero. The tangential biaxial stress at the interface in Li_xSi (σ_t^{LixSi}) is equal to the compressive yield strength ($-\sigma_Y$) assuming plastic deformation in the lithiated Si[21]. Before the contact, mechanical equilibrium requires the tangential biaxial stress at the interface in crystalline Si (σ_t^{Si}) to be related to σ_t^{LixSi} and the ratio of the thickness of Li_xSi (t_{LixSi}) to the half thickness of crystalline Si (t_{Si}), as follows:

$$\sigma_t^{Si} = \frac{t_{Li_xSi}}{t_{Si}}\sigma_Y = \frac{4t_1}{t_0 - t_1}\sigma_Y = \frac{4t_1/t_0}{1 - t_1/t_0}\sigma_Y \tag{3}$$

Then, the mean stresses at the interfaces in the crystalline Si core and in the Li_xSi layer are expressed as:

Before contact: $\sigma_m^{Si} = \frac{\sigma_{t1}^{Si} + \sigma_{t2}^{Si}}{3} = \frac{2\sigma_t^{Si}}{3}$, $\sigma_m^{Li_xSi} = \frac{\sigma_{t1}^{Li_xSi} + \sigma_{t2}^{Li_xSi}}{3} = -\frac{2\sigma_Y}{3}$ (4)

where $\sigma_{t1}^{Si} = \sigma_{t2}^{Si} = \sigma_t^{Si}$ and $\sigma_{t1}^{LixSi} = \sigma_{t2}^{LixSi} = \sigma_t^{LixSi} = -\sigma_Y$. After contact, the displacement of each of the two surfaces is limited to half of the initial gap, $g/2$ and a normal stress at the interface, σ_n develops on the {110} interface in crystalline Si and on the Li_xSi layer (Fig 3b). Since the deformation is fully constrained by the contact and the interfacial compatibility, additional plastic deformation is no longer

possible and additional lithiation induced strain must be accommodated by the elastic deformation. In this case, the stress state in the Si core and Li_xSi layer can be computed by the superposition of the normal stress. The tangential stress at the interface in Li_xSi is then determined from the von Mises yield criterion, as follows

$$\sigma_t^{Li_xSi} = \sigma_n - \sigma_Y \tag{5}$$

From the force equilibrium and displacement constraint from the gap, the tangential stress at the interface in crystalline Si is then expressed as:

$$\sigma_t^{Si} = \frac{t_{Li_xSi}}{t_{Si}}\sigma_t^{Li_xSi} = \frac{t_1 + 0.5g}{t_0 - t_1}\sigma_t^{Li_xSi} = \frac{t_1/t_0 + 0.5\,g/t_0}{1 - t_1/t_0}\sigma_t^{Li_xSi} \tag{6}$$

Then, the mean stresses in crystalline Si and Li_xSi at the interface would be given as:

$$\text{After contact, } \{110\}: \quad \sigma_m^{Si} = \frac{2\sigma_t^{Si} + \sigma_n}{3}, \quad \sigma_m^{Li_xSi} = \frac{2\sigma_t^{Li_xSi} + \sigma_n}{3} \tag{7}$$

where, as shown below, σ_n is a negative quantity. Considering the limitation that the surface displacement due to swelling of Li_xSi along the <110> direction is equal to half of the initial gap, *g/2* and assuming that elastic deformation accommodates further growth of the layer and that lateral flow of Li_xSi is suppressed, the normal stress (σ_n) that develops after contact as a function of the extent of continued lithiation may be estimated using a simple uniaxial stress analysis. For this analysis the dimension t_1, the thickness of the consumed Si layer, may be taken as a measure of the extent of lithiation. As shown in the Supplementary Note 1, the axial stress that develops after contact can be calculated as:

$$\sigma_n = -\left[E_{Si}E_{Li_xSi}\left(3\frac{t_1}{t_0} - \frac{g}{2t_0}\right)\right] \Big/ \left[E_{Li_xSi} + \left(4E_{Si} - E_{Li_xSi}\right)\frac{t_1}{t_0}\right], \qquad \text{when } \; 3\frac{t_1}{t_0} \; 3 \; \frac{g}{2t_0} \tag{8}$$

where E_{Si} and E_{LixSi} are Young's modulus of crystalline Si and Li_xSi, respectively.

In the estimation of the stress, the considered yield strength of Li_xSi (σ_Y) is 1.0 GPa, and E_{Si} and E_{LixSi}

are 180 and 35 GPa, respectively[15,16]. The ratio of the gap and initial thickness of crystalline Si (g/t_0) are 0.3, 0.6, 1.2, and 2.4. Figs. 3c-e show tangential, normal, and mean stresses and the change of free energy due to mechanical stress versus the extent of lithiation (t_1/t_0) when g/t_0 is 0.3 (see also Supplementary Fig. 3a-d). The normal stress (σ_n) acting in both crystalline Si and Li_xSi rapidly becomes more compressive after the contact (red solid line in Fig. 3c). The compressive tangential stress at the interface in Li_xSi (σ_t^{LixSi}) develops after the contact together with the compressive normal stress (dashed line in Fig. 3c). The tangential stress at the interface in crystalline Si (σ_t^{Si}) rapidly increases after the contact as the tangential stress at the interface in Li_xSi decreases (black solid line in Fig. 3c). The mean stresses at the interfaces in crystalline Si and Li_xSi (σ_m^{Si} and σ_m^{LixSi}) for a given extent of lithiation (t_1/t_0) are calculated by equations (3-8) as shown in Fig. 3d. σ_m^{LixSi} is constant before contact and σ_m^{Si} increases slightly due to the increase of the tangential stress in crystalline Si upon lithiation (see also Supplementary Fig. 3c). After contact, σ_m^{LixSi} becomes more compressive following the trend of the normal stress. Assuming that $\Omega^{LixSi}/\Omega^{Si}$ is 4 and x is 3.75 ($Li_{3.75}Si$) considering a 400% volume change for fully lithiated Si at room temperature, Fig. 3e shows the change of free energy due to mechanical stress at the interface (ΔG_σ) for the extents of lithiation (t_1/t_0) corresponding to the mean stresses shown and explains how mechanical clamping along the <110> direction suppresses the lithiation of crystalline Si at the interface. Before the contact, ΔG_σ slightly increases from 0.09 eV to 0.094 eV and the lithiation along <110> direction is continued spontaneously since the free energy of Li deposition versus lithiation of Si ($\Delta G_r^{Li\text{-}LixSi}$) is 0.18 eV[40]**.** After the contact, as σ_n and σ_t^{LixSi} become more compressive, the increasing ΔG_σ reduces the gap of the net driving force between the lithiation of Si and Li deposition. Then, finally, ΔG_σ exceeds $\Delta G_r^{Li\text{-}LixSi}$ as marked as a red dot in Fig. 3e and lithiation of Si is stopped at the interface where the physical interaction induces a sufficiently big compressive normal stress (<110> direction in the experiment). After this point is reached Si is lithiated mainly along the other direction,

free from the physical contact (<100> direction in the experiment). From the point of contact to the point at which the reaction is stopped the extent of lithiation (t_1/t_0) changes by only 0.0025 (red dashed line), which means that mechanical contact can effectively prohibit further lithiation right after the contact is made. For larger gaps, the lithiation after contact goes further but is still less than 0.4% (see Supplementary Fig. 3d).

Mechanical fracture

Mechanical clamping of a Si structure upon lithiation affects the fracture behavior as well as the preferred direction of lithiation. Fig. 4 shows how mechanical clamping enhances the fracture resistance of the lithiated Si pillar. The unclamped Si pillar has a critical diameter of ~300 nm for fracture and the fracture ratio is almost 100 % when its diameter is larger than 300 nm [6]. However, the clamped <110> Si pillar with a diameter of 1 μm and a gap of 300 nm expands along the unclamped <100> directions and only a few pillars show noticeable cracking after lithiation (Fig. 4a-b). But the clamped pillar shows size dependent fracture upon lithiation just as the unclamped pillar does. When the diameter of the pillars increases to 2.2 μm with a 300 nm gap, the pillars still show expansion along <100> direction but then significant cracks are found between <110> and <100>directions (Fig. 4c-d). The statistical study of fracture ratio of the pillars can clearly show different fracture resistance for clamped and unclamped cases (Fig. 4e). The fracture ratio is obtained by counting the number of fractured pillars with various diameters (see Supplementary Fig. 4). The unclamped pillar shows a significant increase of fracture ratio from 0 to 99 % when the diameter increases from 0.26 to 0.39 μm, as reported in our previous study[20]. In contrast, here the fracture ratio is 0 % when the diameter of the clamped pillar is 0.55 μm and only gradually increases as the diameter increases. When the diameters of clamped pillars are 1, 1.4, and 2.2 μm, the fracture ratios are 12, 19, and 52 %, respectively. The diameter of the largest pillar in the test is

about 7 times of critical diameter of the unclamped pillar for fracture, but half of them have not fractured.

A finite element analysis can be used to explain how mechanical clamping affects the stress distribution and enhances fracture resistance of the Si pillar upon lithiation. For this analysis the initial diameter of the simulated <110> Si pillar is 550nm (dashed circle) and the gap between the pillar and the wall is 160nm (see Fig. 4f). For the lithiation, the artificial moving boundaries between crystalline Si and Li_xSi have a marching speed ratio of 5:1 along <110> and <100> directions, respectively, as in our previous analysis[30] (see supplementary Fig. 5). For the clamped pillar, the movement of the interface along the <110> direction is forced to stop after full contact is made (contact area does not increase). The volume change of lithiated Si is 400% and the considered mechanical properties are same with the analysis above (see Supplementary Note 2 and supplementary Table 1). Fig. 4f compares the estimated in-plane principal stress of a fully lithiated Si pillar with/without mechanical clamping. As our previous studies have shown, the unclamped pillar shows a concentration of tensile stress as high as 2GPa on the top and bottom of the pillar along the <100> direction [20]. The clamped pillar shows the concentration of tensile stress on the surface of the pillar along the diagonal direction between <110> and <100> after the contact with the wall (see also Supplementary Movies 6 and 7). But the maximum tensile stress for the clamped pillar is only as high as 1.2GPa. The lower maximum tensile stress for the clamped pillar compared to that for the unclamped pillar is caused by the compressive stresses associated with mechanical clamping, which leads to an enhanced fracture resistance, as shown in the experiment (Fig. 4e). The mechanical clamping also changes the fracture location. The statistical study of the population of crack locations on the pillar (Fig. 4f) shows that the favored fracture site of the clamped pillar is located along a diagonal between the <110> and <100> directions (see Supplementary Fig. 6).

Discussion

Fundamental studies of Si as a negative electrode material for electrochemical reactions with Li have revealed how the mechanical stress caused by the large volume changes associated with the reaction plays an important role in both control of the reaction and fracture of the Si structures. However, while most studies have focused on the mechanical behavior of individual Si particles, wires or pillars, Si anodes in batteries are composed of clusters of particles or wires of different shapes all in a confined space. In the present work, *ex situ* SEM and *in situ* TEM techniques were used to study the effects of mechanical interactions of well-defined crystalline Si nanopillar pairs during lithiation and how those interactions affect both the reaction kinetics and the fracture behavior. When the Si structure is mechanically clamped by adjacent rigid walls along <110> directions, the reaction in that direction is suppressed by compressive stresses that reduce the driving force for lithiation in that direction. This causes lithiation to occur in the transverse, <100>, direction which is not favored for unconstrained particles, wires or pillars. Based on our observations, we can imagine that the overall lithiation behavior of real electrodes involves the swelling Si particles that push each other and translate to empty space until clamped conditions are reached. After the clamping of the most favored lithiation directions, the reactions at the contact points are suppressed by compressive stresses and the other directions free from the clamping are consequently lithiated, much like filling the empty space (see Supplementary Fig. 7). Mechanical clamping of lithiated Si also dramatically enhances the fracture resistance and increases the critical size for fracture because compressive stresses at the contact point compensate the concentrated tensile stress at the free surface. Thus, we can anticipate that the Si particles in the clusters in Li-ion batteries become more resistant to fracture than the individual Si structures that have received most attention. Although compressive stresses enhance the fracture resistance and promote filling of the empty space in the Si particle clusters, a space considering 400% volume change to allow complete

lithiation is required to use maximum charge capacity of Si anode. Hence, further investigation is necessary to optimize the particle size and the empty space preventing mechanical fracture as well as allowing complete lithiation. In addition, since pristine crystalline Si remains amorphous after the first lithiation, the study of mechanical interaction of amorphous Si during electrochemical reaction is also demanded. Nevertheless, we believe that this study of mechanical interaction of lithiated Si pillars provides better idea of how Si structure will be studied and designed in the electrode level for high performance Li-ion batteries.

Methods

Fabrication of Si nanopillar. <110> crystalline Si pillar with walls was fabricated by e-beam lithography and dry etching (see Supplementary Fig. 1). Poly methyl methacrylate (PMMA) pattern for the mask of dry etching was defined on <110> single crystalline Si wafer by e-beam lithography (Nova NanoSEM 450 Scanning Electron Microscope, FEI). Then, the Si wafer is etched by deep reactive ion etching (Deep RIE) process for 10~15 minutes with SF_6 gas for etching and C_4H_8 gas for passivation (Surface Technology Systems Co.). Finally, acetone and methanol cleaning removed PMMA pattern on the etched Si pillar and walls. For *in situ* TEM study, Si wafer was cut along <110> direction by K&S 775 Wafer Dicing Saw and PMMA pattern was defined on the cutting edge of the wafer (see Supplementary Fig. 2). The last fabrication process was same as mentioned above.

Electrochemical characterization by use of *ex situ* SEM. A piece of Si wafer with the pillar and wall structures as a working electrode was assembled with a polymer separator (Nagase & Co. Ltd.) and Li metal foil as a counter and reference electrode to build a sandwich structure of a half-cell (see Supplementary Fig. 1i). BioLogic VMP3 multi-channel battery tester swept voltage of the cell down to

10 mV vs. Li/Li^+ with a scan rate of 0.1 mV s^{-1} and it is was held for more than 10 hours for complete lithiation of the pillars. After the lithiation, the cell was disassembled and the electrode containing lithiated pillars was washed with acetonitrile to remove residual electrolyte in Ar filled glove box. The sample was sealed in a vial in the glove box to avoid the oxidation of the sample and transferred to the vacuum chamber in SEM within 15 s.

***In situ* TEM observation.** The *in situ* electrochemical test was carried out in an FEI Titan 80-300 environmental TEM at the acceleration voltage of 300 kV. Nanofactory Instruments Dual-Probe STM-TEM *in situ* sample holder was employed to apply bias between Si nanopillars and Li metal counter electrode. During transferring the Li metal electrode inside TEM, the electrode was exposed to air for about 5 s to create a thin Li_2O layer of about 20 nm functioning as a solid electrolyte. A relative bias of -4 or -5 V was applied between the two electrodes, which caused Li^+ ions to be transferred to Si nanopillar electrode through the electrolyte.

References

1. Chan, C. K. *et al.* High-performance lithium battery anodes using silicon nanowires. *Nat. Nanotechnol.* **3,** 31–35 (2008).

2. Wu, H. & Cui, Y. Designing nanostructured Si anodes for high energy lithium ion batteries. *Nano Today* **7,** 414–429 (2012).

3. Whittingham, M. S. Materials challenges facing electrical energy storage. *MRS Bull.* **33,** 411–421 (2008).

4. McDowell, M. T., Lee, S. W., Nix, W. D. & Cui, Y. Understanding the lithiation of silicon and other alloying anodes for lithium-ion batteries. *Adv. Mater.* **25,** 4966–4985 (2013).

5. Kasavajjula, U., Wang, C. & Appleby, a. J. Nano- and bulk-silicon-based insertion anodes for lithium-ion secondary cells. *J. Power Sources* **163,** 1003–1039 (2007).

6. Lee, S. W., McDowell, M. T., Berla, L. a, Nix, W. D. & Cui, Y. Fracture of crystalline silicon nanopillars during electrochemical lithium insertion. *Proc. Natl. Acad. Sci. U. S. A.* **109,** 4080–4085 (2012).

7. Wu, H. *et al.* Stable cycling of double-walled silicon nanotube battery anodes through solid-electrolyte interphase control. *Nat. Nanotechnol.* **7,** 310–315 (2012).

8. Liu, N. *et al.* A yolk-shell design for stabilized and scalable Li-ion battery alloy anodes. *Nano Lett.* **12,** 3315–3321 (2012).

9. Liu, N. *et al.* A pomegranate-inspired nanoscale design for large-volume-change lithium battery anodes. *Nat. Nanotechnol.* **9,** 187–192 (2014).

10. Magasinki, A. *et al.* High-performance lithium-ion anodes using a hierarchical bottom-up approach. *Nat. Mater.* **9,** 353–358 (2010).

11. Yao, Y. *et al.* Interconnected silicon hollow nanospheres for lithium-ion battery anodes with long cycle life. *Nano Lett.* **11,** 2949–2954 (2011).

12. Ge, M. *et al.* Large-scale fabrication, 3D tomography, and lithium-ion battery application of porous silicon. *Nano Lett.* **14,** 261–268 (2014).

13. Shenoy, V. B., Johari, P. & Qi, Y. Elastic softening of amorphous and crystalline Li–Si Phases with increasing Li concentration: A first-principles study. *J. Power Sources* **195,** 6825–6830 (2010).

14. Zhao, K. *et al.* Lithium-assisted plastic deformation of silicon electrodes in lithium-ion batteries: a first-principles theoretical study. *Nano Lett.* **11,** 2962–2967 (2011).

15. Sethuraman, V. a., Chon, M. J., Shimshak, M., Srinivasan, V. & Guduru, P. R. In situ measurements of stress evolution in silicon thin films during electrochemical lithiation and delithiation. *J. Power Sources* **195,** 5062–5066 (2010).

16. Ratchford, J. B. *et al.* Young's modulus of polycrystalline Li22Si5. *J. Power Sources* **196,** 7747–7749 (2011).

17. Hertzberg, B., Benson, J. & Yushin, G. Ex-situ depth-sensing indentation measurements of electrochemically produced Si–Li alloy films. *Electrochem. commun.* **13,** 818–821 (2011).

18. Pharr, M., Suo, Z. & Vlassak, J. J. Measurements of the fracture energy of lithiated silicon electrodes of Li-ion batteries. *Nano Lett.* **13,** 5570–5577 (2013).

19. Huggins, R. A. & Nix, W. D. Decrepitation model for capacity loss during cycling of alloys in rechargeable electrochemical systems. *Ionics (Kiel).* **6,** 57–63 (2000).

20. Ryu, I., Lee, S. W., Gao, H., Cui, Y. & Nix, W. D. Microscopic model for fracture of crystalline Si nanopillars during lithiation. *J. Power Sources* **255,** 274–282 (2014).

21. Zhao, K. *et al.* Concurrent Reaction and Plasticity during Initial Lithiation of Crystalline Silicon in Lithium-Ion Batteries. *J. Electrochem. Soc.* **159,** A238–A243 (2012).

22. Yang, H. *et al.* A chemo-mechanical model of lithiation in silicon. *J. Mech. Phys. Solids* **70,** 349–361 (2014).

23. Pharr, M., Zhao, K., Wang, X., Suo, Z. & Vlassak, J. J. Kinetics of initial lithiation of crystalline silicon electrodes of lithium-ion batteries. *Nano Lett.* **12,** 5039–5047 (2012).

24. Ryu, I., Choi, J. W., Cui, Y. & Nix, W. D. Size-dependent fracture of Si nanowire battery anodes. *J. Mech. Phys. Solids* **59,** 1717–1730 (2011).

25. Beaulieu, L. Y., Hatchard, T. D., Bonakdarpour, A., Fleischauer, M. D. & Dahn, J. R. Reaction of Li with alloy thin films studied by in situ AFM. *J. Electrochem. Soc.* **150,** A1457–A1464 (2003).

26. Rhodes, K., Dudney, N., Lara-Curzio, E. & Daniel, C. Understanding the degradation of silicon electrodes for lithium-ion batteries using acoustic emission. *J. Electrochem. Soc.* **157,** A1354–A1360 (2010).

27. Li, J. & Dahn, J. R. An in situ X-ray diffraction study of the reaction of Li with crystalline Si. *J. Electrochem. Soc.* **154,** A156–A161 (2007).

28. Chon, M. J., Sethuraman, V. A., McCormick, A., Srinivasan, V. & Guduru, P. R. Real-time measurement of stress and damage evolution during initial lithiation of crystalline silicon. *Phys. Rev. Lett.* **107,** 045503 (2011).

29. Goldman, J. L., Long, B. R., Gewirth, A. a. & Nuzzo, R. G. Strain anisotropies and self-limiting capacities in single-crystalline 3D silicon microstructures: models for high energy density lithium-ion battery anodes. *Adv. Funct. Mater.* **21,** 2412–2422 (2011).

30. Lee, S. W., McDowell, M. T., Choi, J. W. & Cui, Y. Anomalous shape changes of silicon nanopillars by electrochemical lithiation. *Nano Lett.* **11,** 3034–3039 (2011).

31. Lee, S. W., Berla, L. a., McDowell, M. T., Nix, W. D. & Cui, Y. Reaction front evolution during electrochemical lithiation of crystalline silicon nanopillars. *Isr. J. Chem.* **52,** 1118–1123 (2012).

32. Nam, S. H. *et al.* Probing the lithium ion storage properties of positively and negatively carved silicon. *Nano Lett.* **11,** 3656–3662 (2011).

33. Berla, L. a., Lee, S. W., Ryu, I., Cui, Y. & Nix, W. D. Robustness of amorphous silicon during the initial lithiation/delithiation cycle. *J. Power Sources* **258,** 253–259 (2014).

34. Liu, X. H. & Huang, J. Y. In situ TEM electrochemistry of anode materials in lithium ion batteries. *Energy Environ. Sci.* **4,** 3844–3860 (2011).

35. McDowell, M. T. *et al.* Studying the kinetics of crystalline silicon nanoparticle lithiation with in situ transmission electron microscopy. *Adv. Mater.* **24,** 6034–6041 (2012).

36. Liu, X. H. *et al.* In situ atomic-scale imaging of electrochemical lithiation in silicon. *Nat. Nanotechnol.* **7,** 749–756 (2012).

37. Liu, X. H. *et al.* Ultrafast electrochemical lithiation of individual Si nanowire anodes. *Nano Lett.* **11,** 2251–2258 (2011).

38. Liu, X. H. *et al.* Size-dependent fracture of silicon nanoparticles during lithiation. *ACS Nano* **6,** 1522–1531 (2012).

39. McDowell, M. T. *et al.* In situ TEM of two-phase lithiation of amorphous silicon nanospheres. *Nano Lett.* **13,** 758–764 (2013).

40. Limthongkul, P., Jang, Y.-I., Dudney, N. J. & Chiang, Y.-M. Electrochemically-driven solid-state amorphization in lithium-silicon alloys and implications for lithium storage. *Acta Mater.* **51,** 1103–1113 (2003).

Acknowledgements

Y.C. acknowledges the support from the Assistant Secretary for Energy Efficiency and Renewable Energy, Office of Vehicle Technologies of the US Department of Energy. H.-W.L. acknowledges support from the Basic Science Research Program through the National Research Foundation of Korea (NRF) funded by the Ministry of Education, Science and Technology under NRF-2012R1A6A3A03038593. I.R. and H.G. acknowledge funding from the US Department of Energy through the DOE EPSCoR Implementation grant no. DE-SC0007074. W.D.N. gratefully acknowledges support from the Office of Science, Office of Basic Energy Sciences, of the U.S. Department of Energy under Contract No. DE-FG02-04ER46163.

Author contributions

S.W.L., H.-W.L., and Y.C. conceived the idea, designed experiments, analyzed data, and wrote the paper. S.W.L. carried out experiments. H.-W.L conducted in situ TEM characterization. I.R. did numerical analysis. W.D.N. and H.G. gave comments of mechanics. All the authors read the paper and made comments.

Additional information

Supplementary Information accompanies this paper at online website.

Competing financial interests

The authors declare no competing financial interests.

Figure legends

Figure 1 | SEM study of the lithiation of a clamped <110> Si nanopillar. a, b, SEM images of <110> Si nanopillar positioned between adjacent rigid walls before **(a)** and after **(b)** lithiation. The electrochemical lithiation of a single pillar was suppressed by compressive stresses between the two rigid walls, which were supposed to be preferably grown to <110> direction as displayed in a schematic diagram **(a)**. **c,** Column chart of dimension change of <110> Si nanopillar along <110> (blue) and <100> (green) direction after lithiation when the pillar is unclamped[30] and clamped. Single <110> Si nanopillar standing alone has preferential lithiation along <110> directions of Si but the clamped Si nanopillar shows further expansion along <100> direction.

Figure 2 | *In situ* TEM study of the lithiation of a clamped <110> Si nanopillar. a, A schematic image of the electrochemical cell configuration for *in situ* TEM observation. E-beam penetrates through <100> direction of Si nanopillar to observe a lateral <110> expansion during lithiation. **b,** SEM image of pristine three pillars with adjacent rigid walls on both sides for in situ TEM observation. **c-e,** Time-series of TEM images of the pillars during lithiation. All scale bars in SEM and TEM images are 500 nm. **f,** The diameters of crystalline Si core and lithiated outer Li_xSi for the time line in the middle of lithiation. The lithiation cannot proceed further along <110> direction against the neighboring pillars due to the mechanical clamping.

Figure 3 | Analytical model of the clamped Si pillar to predict the change of the driving force of the reaction. a, A schematic view of <110> crystalline Si with wall fixed at the end. The scheme represents morphological expansion and induced stresses during lithiation of <110> pillars and walls before the

physical contact ('Before contact', $t_2 < g/2$). **b,** A schematic view of the one side of Si pillar contacted with the wall physically ('After contact', $t_2 \geq g/2$). The displacement of lithiated Si is confined as a half of the gap ($g/2$). **c,** Normal (σ_n) and tangential (σ_t) stress at the interfaces in the crystalline Si and Li_xSi for the depth of lithiation (t_1/t_0) when g/t_0 is 0.3. **d,** Mean stress (σ_m) at the interfaces in the crystalline Si (solid) and Li_xSi (dotted) for the depth of lithiation (t_1/t_0) when g/t_0 is 0.3. **e,** Corresponding change of free energy due to mechanical stress (ΔG_σ) for the depth of lithiation (t_1/t_0) when g/t_0 is 0.3. Black dash line represents free energy of Li deposition versus free energy of lithiation of Si ($\Delta G_r^{Li\text{-}LixSi}$). Red vertical lines indicate the contact and reaction stoppage upon lithiation of Si, respectively.

Figure 4 | Improved fracture resistance of the clamped Si nanopillar upon lithiation. a, b, SEM images of crystalline <110> Si pillar of 1 μm diameter and the walls with gap of 300 nm. The pillar is clamped by the walls and expanded along <100> direction upon lithiation. Significant crack is not found. **c, d,** SEM images of crystalline <110> Si pillar of 2.2 μm diameter and the walls with gap of 300 nm. After lithiation, the cracks are found between <110> and <100> directions as indicated by red arrows. All scale bars are 1 μm. **e,** Column chart of the fracture ratio of the clamped <110> Si pillars for various diameters. To compare the effect of mechanical clamping for the fracture resistance, the fracture ratio of unclamped <110> pillar is shown as red columns[20]. **f,** Finite element analysis of in-plane principal stress of unclamped (left) and clamped (right) <110> Si pillar after full lithiation. Initial diameter is 550nm (dot circle) and lateral displacement of clamped pillar is confined to 160nm (solid line). **g,** Column chart of the population of the fracture location as an angle of the crack in the clamped <110> Si pillar upon lithiation (blue). The population of the fracture location of the unclamped <110> pillar (red) compares how mechanical clamping changes the fracture behavior[6].

Figure 1

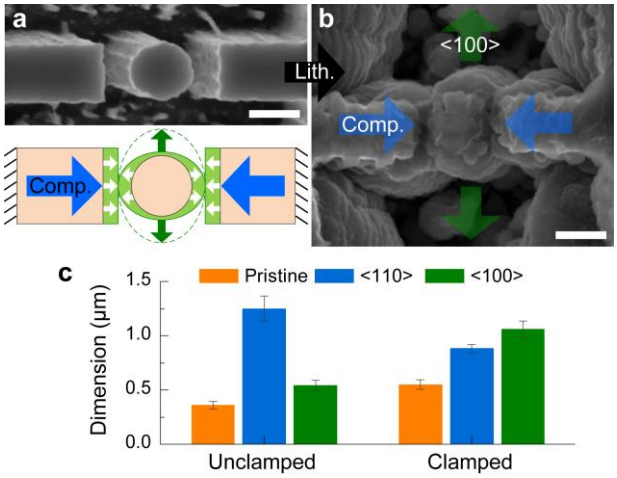

Figure 2

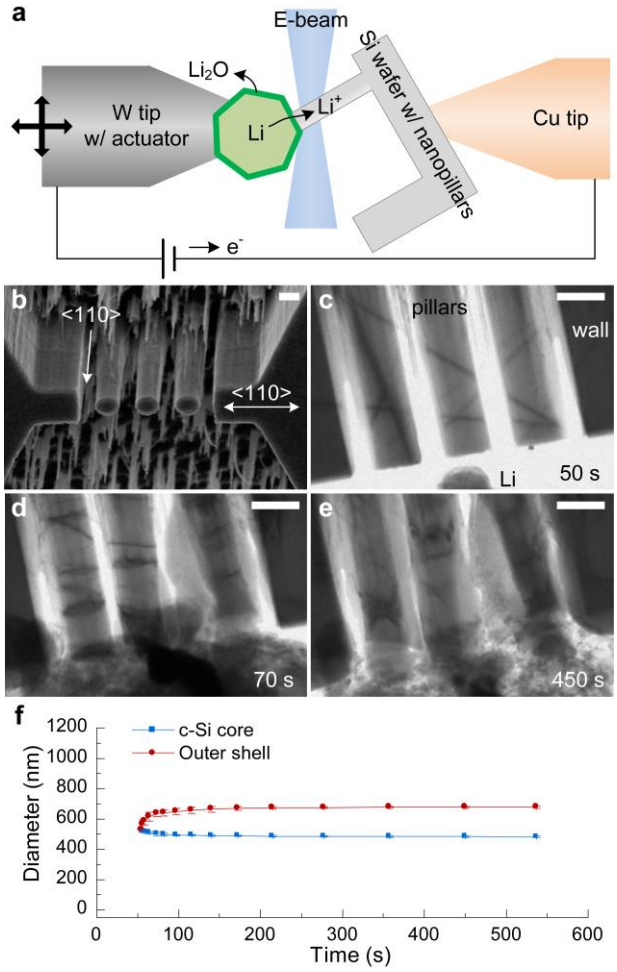

Figure 3

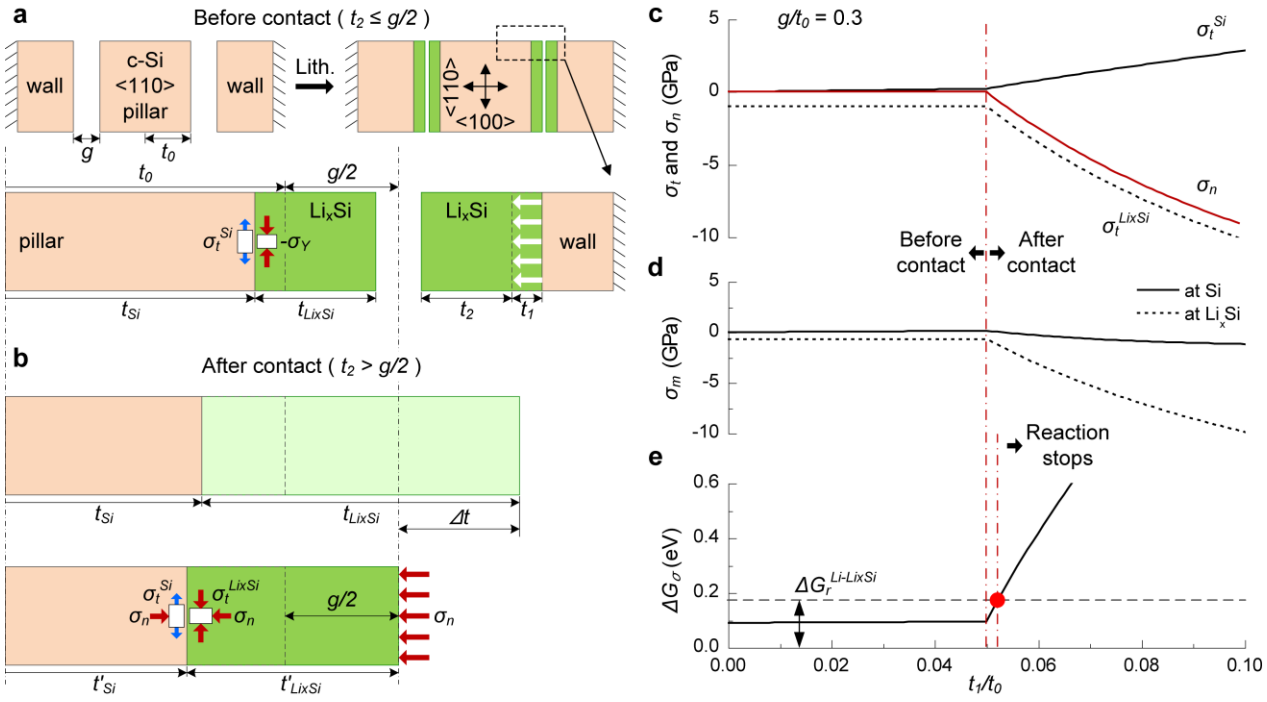
a
Before contact ($t_2 \le g/2$)
wall
c-Si <110> pillar
wall
Lith.
<110>
<100>
g
t_0
t_0
g/2
pillar
σ_t^{Si}
$-\sigma_Y$
Li_xSi
Li_xSi
wall
t_{Si}
t_{LixSi}
t_2
t_1
b
After contact ($t_2 > g/2$)
t_{Si}
t_{LixSi}
Δt
σ_t^{Si}
σ_t^{LixSi}
σ_n
g/2
σ_n
t'_{Si}
t'_{LixSi}
c
g/t_0 = 0.3
σ_t^{Si}
σ_n
σ_t^{LixSi}
σ_t and σ_n (GPa)
Before contact
After contact
d
at Si
at Li_xSi
σ_m (GPa)
e
Reaction stops
$\Delta G_r^{Li\text{-}LixSi}$
ΔG_σ (eV)
t_1/t_0

Figure 4

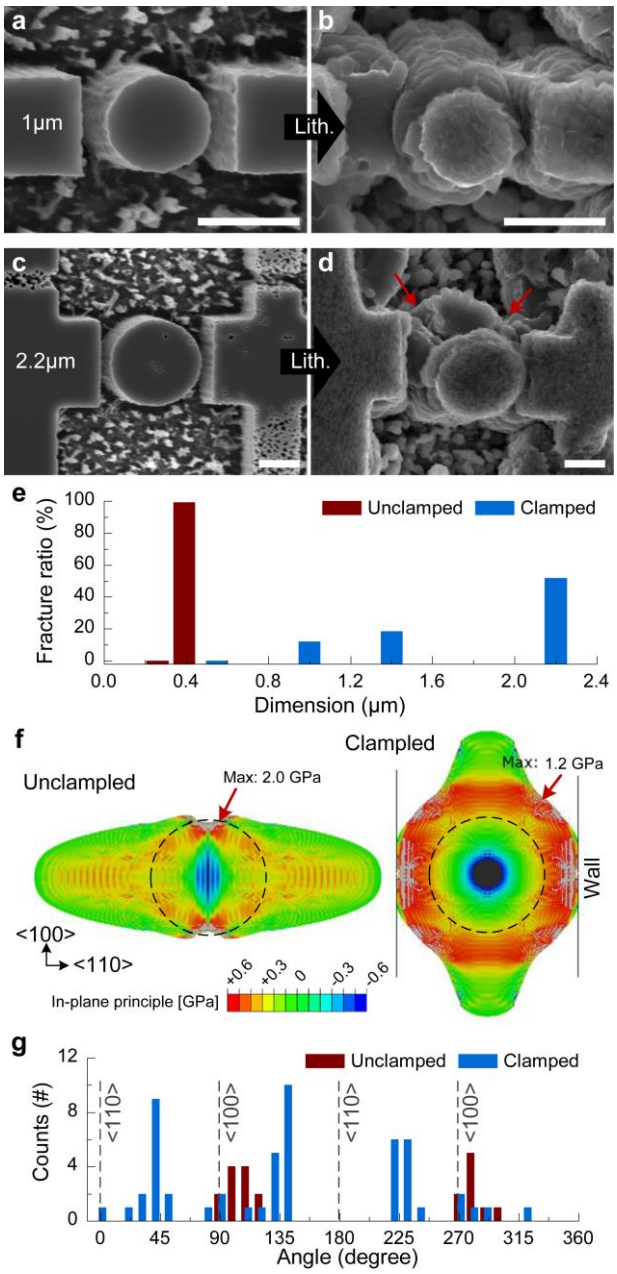
a
1μm
Lith.
b
c
2.2μm
Lith.
d
e
Unclamped
Clamped
Fracture ratio (%)
Dimension (μm)
f
Unclamped
Max: 2.0 GPa
Clampled
Max: 1.2 GPa
Wall
<100>
<110>
In-plane principle [GPa]
+0.6
+0.3
0
-0.3
-0.6
g
Unclamped
Clamped
Counts (#)
Angle (degree)
<110>
<100>
<110>
<100>